

Research Strategy

A. Significance

In this project, we will conduct a brain-wide survey of neuronal cell-types, taking into account morphological, electrical, biophysical, molecular, and computational properties of neurons in the mouse.

Importance of the problem: Cell-type classification is one of the major challenge areas in the BRAIN initiative. Determining the cell-type and their subtypes in the brain is a necessary first step toward a full-blown connectomics study of the brain (Bota and Swanson 2007). We cannot infer the function of brain circuits based on connections alone; we need to know the functional properties of the circuit elements (electrical, molecular, and biophysical).

Critical barriers in the context of current state-of-the-art: Critical barriers to brain-wide cell-type classification are discussed below in the context of current state-of-the-art.

Critical barrier 1: Lack of dense sampling of detailed (sub-micrometer resolution) neuronal morphology data aligned with molecular data. Connectomics research today is focused mostly on connection data acquisition using different imaging modalities: diffusion MRI (dMRI; Hagmann et al. 2008, 2007; Johansen-Berg and Rushworth 2009; Van Essen et al. 2012), light and fluorescence microscopy (Keller et al. 2008; Li et al. 2010; Mayerich et al. 2008b; Ragan et al. 2012; Tsai et al. 2003), and electron microscopy (Anderson et al. 2011; Denk and Horstmann 2004; Hayworth et al. 2006). Large collections of connectivity data based on thousands of tracer injections (Hintiryan et al. 2012; Mitra 2012) and based on dMRI (Human Connectome Project: Van Essen et al. 2012) are becoming available. However, most of the analysis considers connectivity alone (Bullmore and Sporns 2009; Hagmann et al. 2008, 2007; Rubinov and Sporns 2010), and only few early studies have looked into cell types, e.g., the work by Helmstaedter et al. (2013) where they studied cell types in the inner plexiform layer of the mouse retina. To complement the connection-oriented research in connectomics with surveys of cell-type, first we need a large collection of neuronal morphology data, densely sampled from across the whole brain. The mouse brain, the subject of study of this proposal, consists of ~100 million neurons (cf. Williams 2000 estimates 75 million). However, NeuroMorpho.org (Halavi et al. 2008), one of the largest collection of reconstructed neuronal morphology, contains only 2,726 neurons for the mouse (as of March 2014), or roughly 0.0027% of the entire population of neurons. On the other hand, traditional histological stains such as Golgi stain, although sparse, can label about 1% of the entire neuronal population. If a Golgi-stained brain can be imaged, digitized, and the neuronal morphologies fully reconstructed, over a 350-fold improvement over the current state-of-the-art collection can be achieved, laying the basis for a large-scale, dense survey of neuronal cell types. Furthermore, imaging of whole transgenic brains and reconstructing the neuronal morphologies can help align morphological variations with molecular variations. Aims 1 and 3 of this work will address this barrier.

Critical barrier 2: Lack of biophysical data relating to cell-type classification. Initial efforts in neuronal cell-type classification were based on the observed morphology of histologically stained neurons (Ramón y Cajal 1995; Woolsey et al. 1975). We now know that electrophysiological (Labarre et al. 2008; Subkhankulova et al. 2010), synaptic (Helmstaedter et al. 2013; Wouterlood et al. 2008), molecular (Bota et al. 2012; Fishell and Heintz 2013), and gene expression properties (Toledo-Rodriguez et al. 2004) can also dictate cell type and sub-type. Biophysical properties such as elasticity are used in non-neuronal cell type classification and have provided important implications for understanding cancer cell heterogeneity (Cross et al. 2007; Hochmuth 2000; Ingber 2003; Suresh 2007). However, such characterizations have not been attempted in neurons, which is an opportunity and a potential barrier. Aim 2 will address this barrier.

Critical barrier 3: Lack of large-scale, actual neuronal morphology-based multicompartmental simulation data relating to cell-type classification. Detailed dendritic morphology alone can reveal important functional information of neurons. It is well known that differences in dendritic morphology can lead to differences in the electrical properties of neurons (Rall 1962; Rall and Agmon-Snir 1998). Furthermore, dendritic morphology can also have an influence on information processing in the neuron (Mel 1994). Thus, if we have a large collection of detailed neuronal morphologies from different cell types, we can study the electrical and information processing properties of neurons, and discover functional sub-types. Large-scale simulations based on realistic, stochastically generated synthetic neuronal populations are available (the Blue Brain Project, Hill et al. 2012; Markram 2006; Perin et al. 2011). However, large-scale, multicompartmental simulations based on actual neuronal morphology have not been attempted, which represents a critical barrier to cell-type classification. Aim 4 will address this barrier.

Critical barrier 4: Lack of a neuroinformatics platform for dense sampling of neuronal morphology and interoperability with existing resources. Fairly large collections of neuronal morphology (NeuroMorpho.org, Halavi et al.

2008) and projections (Allen Mouse Connectivity Atlas [Allen Institute for Brain Science 2012]; mouse connectome project [Hintiryan et al. 2012; Zingg et al. 2014]; brain architecture project [Mitra 2012]) exist. Furthermore, whole-brain gene expression atlases are made publicly available by the Allen Institute for Brain Science (Lein et al. 2007). However, there is a lack of dense surveys of neuronal morphologies and their distributions across the brain, and a lack of interoperability with existing resources that could complement morphological collections with structural (connectivity) and functional (gene expression) information. Aim 5 will address this barrier.

Specific aims and their expected outcomes:

- **Aim 1: Morphological survey of neuronal cell types across major cortical and subcortical nuclei in the mouse brain.** We expect to obtain a dense sampling (~1%, or ~750,000) of fully reconstructed neuronal morphologies from the mouse brain (Golgi preparation).
- **Aim 2: Measurement of biophysical properties of different morphological cell types of neurons.** We expect to measure elasticity of ~100,000 neurons of different types sampled across the whole mouse brain and correlate the single-cell elasticity measurement to other cell-type-specific neuronal properties. Whether correlations can be found or not is an open question at this point.
- **Aim 3: Molecular characterization of different morphological cell types.** We expect to be able to infer broad cell-type classifications (GABAergic vs. non-GABAergic) based on the morphology and molecular properties. The method we developed here can open the way to industrialized (high-throughput, high-resolution) molecular characterizations of whole mouse brains.
- **Aim 4: Computational characterization of different morphological cell types.** We expect our efficient multicompartmental simulation algorithms to allow fast and complete electrophysiological characterization of different and similar morphological cell types. Our algorithm can routinely simulate on the order of one million neurons, so we expect to be able to simulate all reconstructed neurons from Aims 1 and 3.
- **Aim 5: Neuroinformatics platform for the exploration and analysis of data from Aims 1 through 4.** We expect our new neuroinformatics platform to allow neuroscience researchers to easily access neuronal morphology and other cell-type-related information from our data, and to conduct cross-linked investigation by pulling gene-expression and connectivity data from third-party data sources.

B. Innovation

We will employ and extend innovative technologies and methods developed in our labs (referenced below) to achieve our aims. Below, for each aim, the main PI and/or Co-I responsible for the aim are identified, and relevant references to preliminary works listed.

- **Aim 1:** We will use the Knife-Edge Scanning Microscope (KESM; Chung et al. 2011; Mayerich et al. 2008b), a novel high-throughput high-resolution physical sectioning microscope developed in our lab, to image whole mouse brains stained with Golgi (PI Choe, Co-I Abbott). We will develop novel vector-tracing methods for 3D reconstruction and validation of neuronal morphology (Co-I Keyser; Han et al. 2009a,b; Mayerich et al. 2008a; Mayerich and Keyser 2009; Mayerich et al. 2008c).
- **Aim 2:** We will develop a microfluidics platform (Han et al. 2005; Hennessy et al. 2011) for high-throughput measurement and sorting of neuronal cell bodies based on their biophysical properties such as elasticity, a cell-classification method that has not been attempted on neurons (Co-I Han). We will assess the correlations between measured biophysical properties and morphological, molecular, and electrophysiological properties from Aims 1, 3, and 4, which in itself is novel.
- **Aim 3:** We will extend our embedding techniques for fluorescently labeled neurons in transgenic mouse brains (cf. Choe et al. 2011). The prepared specimen will be subsequently imaged with the KESM (PI Choe) to provide broad categorization of neuronal cell-types, e.g., GABAergic vs. non-GABAergic (Co-I Winzer-Serhan and Co-I Abbott). For reconstruction, we will use the same algorithms developed in Aim 1.
- **Aim 4:** We will develop novel algorithms for efficient multicompartmental simulations based on telescopic projective integration and parallelization. Based on the reconstructed neuronal morphologies from Aims 1 and 3, we will conduct a large-scale multicompartmental simulation study of electrophysiological properties of different types of neurons (Co-I Li; see Yan and Li 2011a,b, 2013; Zhang et al. 2012).
- **Aim 5:** We will extend our novel web-based light-weight mouse brain atlas (the KESM Brain Atlas <http://kesm.org>; Chung et al. 2011; Eng and Choe 2008) to incorporate reconstructed neuronal morphology and register the data to standard coordinate spaces such as the Waxholm space and the Allen reference coordinate system for integrative operation (PI Choe).

C. Approach

C.1. Aim 1: Morphological survey of neuronal cell types across major cortical and subcortical nuclei in the mouse brain.

Sub-Aim 1.1. KESM Imaging: For this aim, we will use the Knife-Edge Scanning Microscope (KESM) for neuronal morphology data acquisition across the whole mouse brain. A fully functional prototype KESM (US patent #6,744,572) (Mayerich et al. 2008b; McCormick 2003, 2004; McCormick and Mayerich 2004) has been designed at Texas A&M University (TAMU) with support from the National Science Foundation (MRI award #0079874: McCormick, PI; IDBR award #1256086: Choe, PI), the Texas Higher Education Coordinating Board (ATP award #000512-0146-2001: Keyser, PI), and the National Institute of Neurological Disorders and Stroke (Award #1R01-NS54252: Choe, PI). The instrument, shown in Fig. 1a, is capable of scanning a complete mouse brain ($\sim 310 \text{ mm}^3$) at $\sim 600 \text{ nm}$ sampling resolution within 100 hours when scanning in full production mode. The instrument comprises four major subsystems: (1) precision positioning stage, (2) microscope/knife assembly, (3) image capture system, and (4) cluster computer.

The specimen, a whole mouse brain, is embedded in a plastic block and mounted atop a three-axis precision positioning stage. A custom diamond knife, rigidly mounted to a massive granite bridge overhanging the three-axis stage, cuts consecutive thin sections from the block. Unlike block face scanning, the KESM concurrently cuts and images (under water) the tissue ribbon as it advances over the leading edge of the diamond knife. A white light source illuminates the rear of the diamond knife, and in turn illuminates the brain tissue at its leading edge, with a strip of intense illumination reflected from the beveled knife-edge, as illustrated in Fig. 1b. Thus, the diamond knife performs two distinct functions: as an optical prism in the collimation system, and as the tool for physically cutting the thin serial sections. The microscope objective, aligned perpendicular to the top facet of the knife, images the transmitted light. A high-sensitivity line-scan camera repeatedly samples the newly cut section, imaging a stripe $20 \mu\text{m}$ -long along the cutting direction on the tissue ribbon and just beyond the knife-edge, prior to subsequent deformation of the tissue ribbon after imaging. Finally, the digital video signal is passed through image acquisition boards and stored in a dedicated cluster computing system. We will use KESM to image whole mouse brains stained in Golgi using methods described in Choe et al. (2011). Data from KESM presented in Figs. 2 and 3 demonstrate the full capability of the KESM for sub-micrometer-resolution histological imaging (voxel resolution = $0.6 \mu\text{m} \times 0.7 \mu\text{m} \times 1.0 \mu\text{m}$, whole brain imaged).

Sub-Aim 1.2. 3D Reconstruction and Validation of Neuronal Morphology: Our goal is to extract from the KESM volume data set the individual geometric structures of interest. We have developed a series of vector-based tracing algorithms (Han et al. 2009b; Mayerich et al. 2008a; Mayerich and Keyser 2008; Melek et al. 2006). Here, we will discuss (Han et al. 2009b) in detail, while leaving open the option of adopting our other approaches (Mayerich et al. 2008a; Mayerich and Keyser 2008) and developing new ones.

Our maximum intensity projection(MIP)-based algorithm provides a general framework for 3D tracing, and one unique strength is that it can use any 2D tracing algorithm as a subroutine. Thus, the overall power of our MIP-based algorithm can be arbitrarily increased by the use of more powerful 2D tracing algorithms. Furthermore, our algorithm takes only about 30% of the time to trace a unit block compared to a full 3D algorithm. The algorithm consists of four steps, starting from a seed point: (1) boundary detection and local axis length determination,

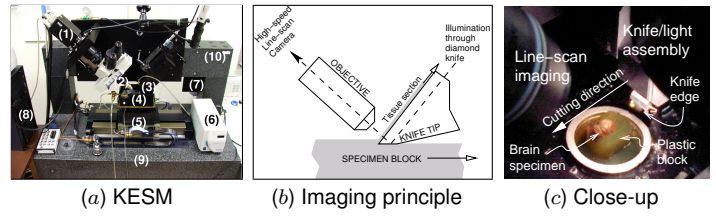


Figure 1: The Knife-Edge Scanning Microscope (KESM). (a) Photo of the KESM instrument showing (1) high-speed line-scan camera, (2) microscope objective, (3) diamond knife assembly and light collimator, (4) specimen tank (for water immersion imaging), (5) three-axis precision air-bearing stage, (6) white-light microscope illuminator, (7) water pump (in the back) for the removal of sectioned tissue, (8) PC server for stage control and image acquisition, (9) granite base, and (10) granite bridge. (b) Specimen undergoing sectioning by knife-edge scanner (thickness of tissue section is $1 \mu\text{m}$). (c) Close-up photo of the line-scan/microscope assembly and the knife/illumination (knife and objective raised to show the brain specimen).

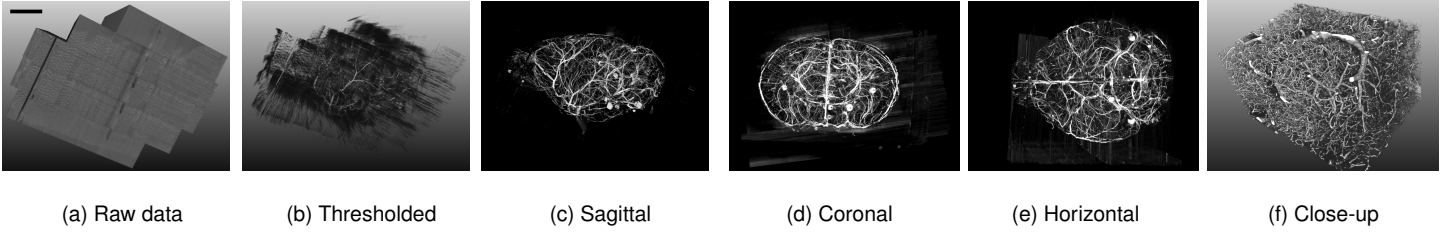


Figure 2: Preliminary Data: Whole-Brain Submicrometer-Resolution Imaging. Various views of the whole-brain Knife-Edge Scanning Microscope vasculature data are shown. (a) shows the raw data block in a sagittal view (scale bar = 1.44 mm). Note that there are 5 tilted columns, with the top of each column facing the upper-left corner of the figure. (b) shows a slightly thresholded version of (a) so that the boundary of the raw data block and the content within can be seen at the same time. (c) is a fully thresholded version of (a) and (b). (d)–(e) show the coronal and horizontal views, respectively. We can clearly see the shape of the brain. (f) shows the intricate details within an 1.5 mm-wide block. Voxel size = $0.6 \mu\text{m} \times 0.7 \mu\text{m} \times 1.0 \mu\text{m}$. Smallest capillaries shown here have a diameter of about 5 μm . This data, although not showing neuronal morphology, demonstrates the capability of KESM to perform submicrometer-resolution imaging of whole mouse brains.

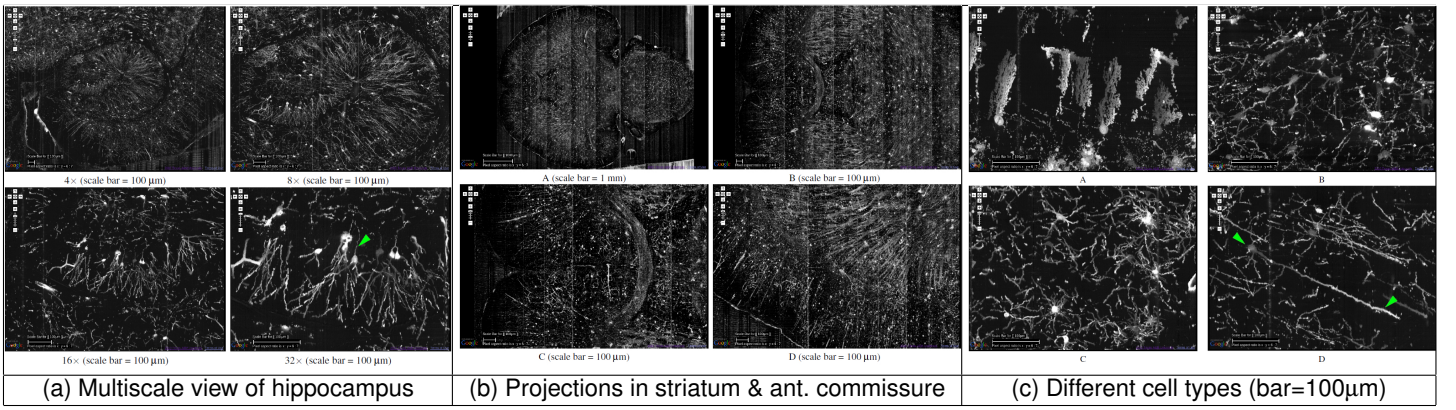


Figure 3: Preliminary Data: Knife-Edge Scanning Microscope Golgi Data. Golgi data from the KESM are shown. (a) Multiscale view of the hippocampus (horizontal section). At the highest resolution, detailed dendritic morphology and traces of axons (green arrowhead) can be observed. (b) Long projections in the anterior commissure and the striatum can also be observed (horizontal section). (c) Different cell types in the cerebellum (A), inferior colliculus (B), thalamus (C), and cortex (D) can be seen. Soma and apical dendrite of a cortical pyramidal cell is marked by green arrowheads. Adapted from Chung et al. (2011). Each image is a composite overlay of twenty 1- μm -thick sections, thus the apparently tangled processes are naturally disambiguated in 3D (see Fig. 11b vs. c).

(2) local volume estimation and local MIP processing, (3) 2D tracing of fiber direction, and (4) 3D fiber direction estimation and adjustment. Fig. 4c shows an overview of our approach (for details see Han et al. 2009b).

(1) First, we define $P_{\text{in}}(\vec{c}, R)$, $P_{\text{out}}(\vec{c}, R)$, and $P_{\text{edge}}(\vec{c}, \tau)$ as the probability of a voxel R-voxels (or τ -voxels) apart from the trace center \vec{c} being inside, outside, or on the edge of the fiber, respectively (Gaussian functions are used). From this, we obtain the edge map $E(\vec{c}, R, \tau) = \frac{1}{3}(P_{\text{in}}(\vec{c}, R - \tau) + P_{\text{out}}(\vec{c}, R + \tau) + P_{\text{edge}}(\vec{c}, \tau))$, and $E(\vec{c}, R) = \max E(\vec{c}, R, \tau)$. The foreground-background boundary along the three axes x , y , and z are found by calculating $\text{argmax}_{R \in [\vec{c}, \dots, \vec{c} + M\vec{e}]} E(\vec{c}, R)$ where M is the maximum fiber width and \vec{e} is the unit vector along one of the principal axes. (2) From these boundaries, the local MIP volume is created, and MIPs are generated on the XY, YZ, and XZ planes. Among these, the projection along the longest fiber direction is ignored since it does not contain fiber direction information. (3) Tracing in 2D is done using a multiscale filter using a Hessian matrix $H_\sigma(x) = \begin{bmatrix} I_{xx}(x) & I_{xy}(x) \\ I_{yx}(x) & I_{yy}(x) \end{bmatrix}$, where $I_{uv}(x) = \sigma^2 \frac{\partial^2 G(x, \sigma) I(x)}{\partial u \partial v}$, where σ is the scale, and $G(x, \sigma)$ is a Gaussian with standard deviation σ , and $I(x)$ is the voxel x in the data volume I . The eigenvector \vec{v}_1 corresponding to the smallest eigenvalue λ_1 indicates the fiber direction. To elaborate, first a fiber-likeness function $V(x, \sigma)$ is defined as 0 when 2nd eigenvalue $\lambda_2 > 0$, and as $\exp\left(-\frac{\lambda_r^2}{2\beta^2}\right)\left(1 - \exp\left(-\frac{S^2}{2c^2}\right)\right)$ otherwise, where $\lambda_r = \frac{\lambda_1}{\lambda_2}$, and

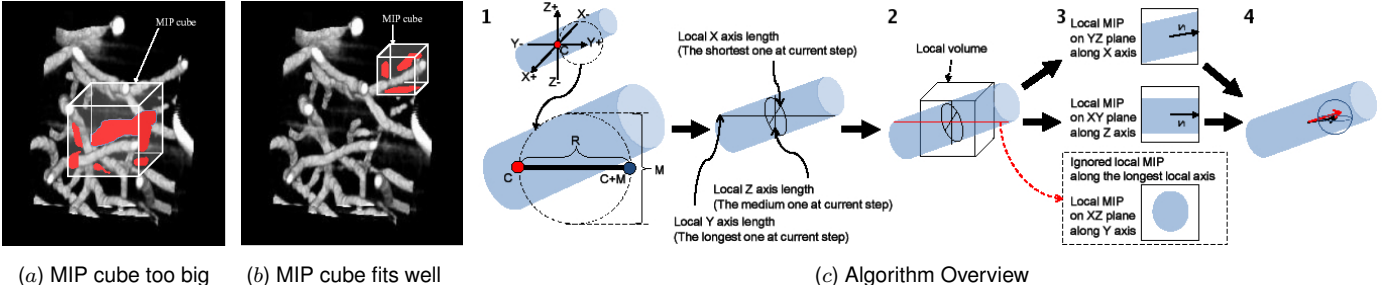


Figure 4: Vector Tracing with Local Maximum-Intensity Projection (MIP). (a-b) Local MIP size has to be small enough for unambiguous, occlusion-free projection (a contains occlusions while b does not). (c) The local MIP-based tracing algorithm. 1. Starting from seedpoint C, longest-axis boundary C+M is found and the boundaries along the other two axes are found. 2. Local MIP cube size is determined. 3. 2D trace is conducted on two of the three MIPs. 4. Results are combined in 3D. Vasculature data are shown for demonstration purpose only.

$S = \sqrt{\sum_{i=1}^2 \lambda_i^2}$, and β and c control the sensitivity of the Hessian filter (0.5 and 0.25, in our experiments). The maximum value along $V(x, \sigma)$ at scale σ gives the eigenvector \vec{v}_1 , which is the fiber direction (see Frangi et al. 1999 for details). (4) Finally, from the 2D tracing on the two MIP planes, the 3D fiber direction is estimated as follows. Assume that XY and YZ were the two chosen planes. Let $\vec{v}_{xy} = (x_1, y_1, 0)$ and $\vec{v}_{yz} = (0, y_2, z_2)$ be the eigenvectors from the two respective MIP planes. The 3D fiber direction is derived as $\vec{v}_{xyz} = (x_1, \frac{y_1+y_2}{2}, z_2)$. From this, the next trace center \vec{c}' can be calculated as $\vec{c}' = \frac{\vec{v}_{xyz}}{\|\vec{v}_{xyz}\|} \rho + \vec{c}$, where ρ is the step size (currently set to 3). The last step corrects for discretization error where we use a momentum operator to calculate the adjusted center $(\bar{x}, \bar{y}, \bar{z}) = \left(\frac{M_{100}}{M_{000}}, \frac{M_{010}}{M_{000}}, \frac{M_{001}}{M_{000}} \right)$, where $M_{pqr} = \int_z \int_y \int_x x^p y^q z^r I(x, y, z) dx dy dz$ (see Boldak et al. 2003 for details).

Our algorithm, due to the use of a 2D Hessian matrix, has computational complexity of $O(n^2)$, while full 3D tracing algorithms based on 3D Hessian matrices have $O(n^3)$ complexity, where n is the scale of the Gaussian filter. In practice, our algorithm takes only about 30% of the time of full 3D versions. Initial implementation of this and related approaches has been successful (Han et al. 2009b; Mayerich et al. 2008a; Mayerich and Keyser 2008; Melek et al. 2006), and we will modify and improve it to trace a wider variety of fibrous data.

Once the neuronal morphologies are fully reconstructed, we need to validate the accuracy. Validation is an important step in any automated reconstruction algorithm (Pham et al. 2000; Warfield et al. 2002; Yoo et al. 2000), however, the scale of our task prevents manual validation, thus we will employ a model-based validation approach using digital phantoms (Pham et al. 2000). Preliminary performance data from our MIP-based tracing algorithm and validation results are shown in Fig. 5.

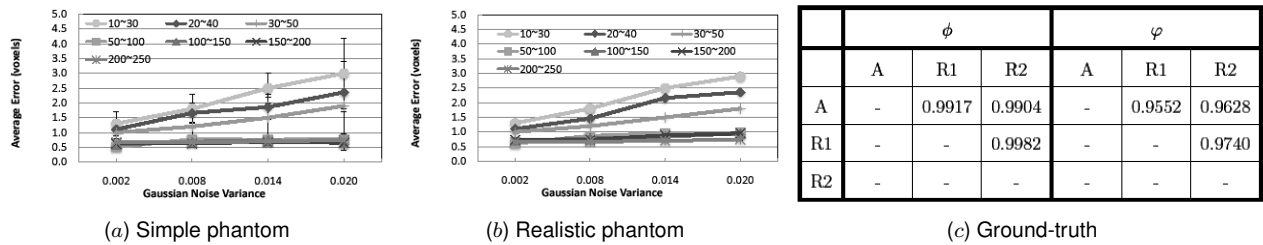


Figure 5: Preliminary Data: Pilot Validation Results. Systematic validation results with varying image contrast and noise level for digital phantoms made of (a) simple, geometric structures and (b) realistic vascular trees are shown. (c) Validation result A against two manual tracing R1 and R2 on real vascular data are shown (ϕ means length difference, and φ means centerline deviation). Values in the table are the correlation coefficients. Note that the results are very similar between a and b that use different types of phantoms, and tracing is close to perfect as can be seen in c. (Pilot results presented in Han et al. (2009b).)

Sub-Aim 1.3. Morphological categorization of reconstructed neurons through statistical analysis: Once the neurons are fully reconstructed, we will use existing morphology-based classification guidelines and ontologies such as BAMS (Bota and Swanson 2007; Swanson and Bota 2010), NeuroLex (Larson and Martone 2013) and the Petilla convention for GABAergic interneurons (Ascoli et al. 2008). We will use file formats used in NeuroMorpho.org (Halavi et al. 2008) and NeuroML (Gleeson et al. 2010) for compatibility. Once the morphometric

properties are summarized for each neuron, we will conduct a large-scale statistical analysis (clustering) similar to the method described in Zawadzki et al. (2009), where “neuromorphological spaces” were inferred based on differences in the geometry of reconstructed neurons. We will also employ Bayesian techniques for cases where expert opinion regarding cell-type can vary (López-Cruz et al. 2014).

C.2. Aim 2: Measurement of biophysical properties of different morphological cell types of neurons

We have previously developed a microfluidic platform that utilizes arrays of microfluidic single cell trapping structures and microfluidic aspiration channels, functioning as a miniaturized high-throughput version of micropipette analysis, for single cancer cell elasticity measurement (Fig. 6a; Kim and Han 2011). This demonstrates that probing and deforming single cells through constricting microstructures enable non-invasive assessment of cell’s elastic properties. We have also developed a series of single-cell analysis platforms based on impedance measurement and applied such systems to characterize breast cancer cell lines from different stages of cancer progression (Han et al. 2007), as well as head and neck cancer cell lines with different metastatic potentials (Cho et al. 2009). These platforms demonstrate our capabilities in developing single-cell analysis microfluidic platforms.

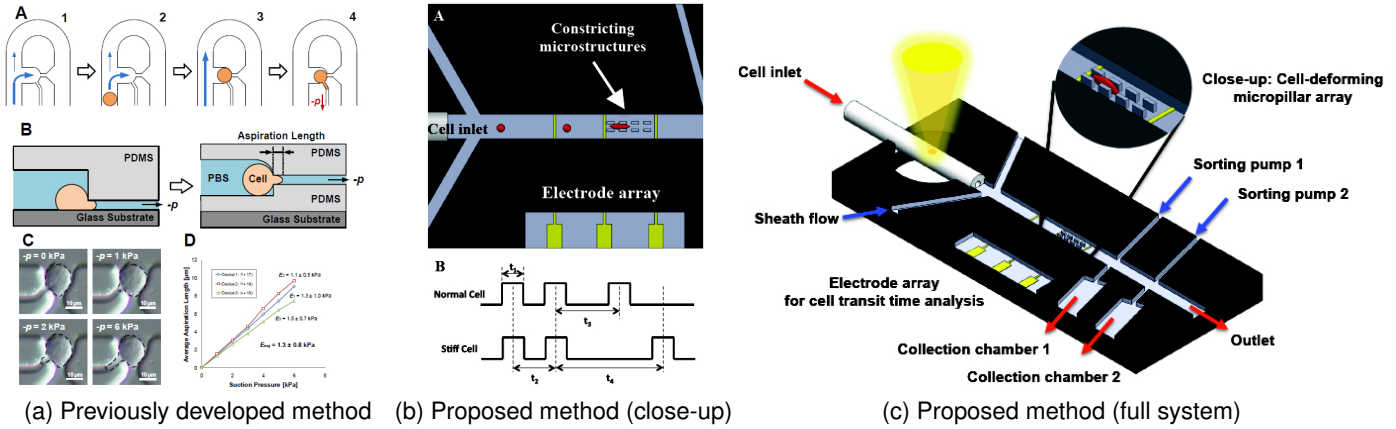


Figure 6: Microfluidic Measurement of Biophysical Properties. Previously developed and proposed methods for the measurement of biophysical properties of cells are shown. (a) Previously developed microfluidic micropipette is used for elasticity measure (A: trapping, B: aspiration, C: Single cancer cell being aspirated, D: Measured cancer cell elasticity [Young’s modulus analysis]). This method, although faster than conventional methos, takes up significant time, so it is not suitable for high-throughput screening. (b) Close-up of the proposed sigle-cell elasticity measurement system is shown in A. Elasticity is measured electronically, by use of a constricting microstructure and logging the transit time as shown in B. Cells with different stiffness will result in different transit time. (c) The integrated microfluidic platform that combines high-throughput single-cell elasticity measurement with high-throughput electric-field based single-cell sorting (see Fig. 7 for cell sorting).

Sub-Aim 2.1: Build a microfluidic prototype for high-throughput cell stiffness measurement. The cell-capture-type cell stiffness analysis we previously developed (as shown in Fig. 6a) provides an accurate way of interrogating single cell’s stiffness. Although faster than conventional methods such as micropipette aspiration or atomic force microscopy (AFM), the throughput is not sufficiently high. The proposed microfluidic chip will be a flow-through type system that can increase the throughput by several orders of magnitude (target of this proposal: 200 cells/s; if higher speeds are needed, cells can be flown into several parallel interrogation channels for simultaneous analysis). The chip will have a microfluidic flow channel with arrays of constricting microstructures positioned in series (Fig. 6b). Thus, overall transit time of cells passing through these microstructures will be slower for stiffer cells and faster for less stiff (i.e., more compressible) cells (Bow et al. 2011). An all-electronic measurement scheme is proposed based on arrays of 3 electrodes with a fourth reference electrode to measure the cell transit time by electrical impedance changes (using a commercial multi-channel impedance analyzer and multiplexer, Zurich Instrument, Inc.). When a cell passes through an electrode, the impedance will change (Fig. 6b). Signals from the first two electrodes will be used to determine the cell flow speed before entering the constricting structure array. This information, combined with the duration of the impedance peak, can be used to

identify the size of the cell. Alternatively, the impedance value can also be used to identify the size of the cell, although decoupling whether the impedance value changes due to cell size or due to differences in cell types have to be characterized by identifying the impedance frequency at which the value is sensitive only to the cell size. The signals from the second and third electrodes can be used to determine the cell transit time through the constricting structure array (Fig. 6b). The frequency at which the electrical impedance is measured will be optimized (100 kHz to 3 MHz) to find a frequency where signal change is maximized during cell passing. The capability to measure both cell size and cell transit time allows decoupling the influence of cell size variation on cell transit time, providing a more accurate means for cell stiffness measurement. Fig. 6c shows the overall system with real-time cell sorting capability.

Sub-Aim 2.2. Develop a data analysis software for automatic cell classification: The entire microfluidic operation will be controlled using LabVIEW-based pump and microvalve control, as well as data acquisition from the electrode arrays. The acquired data (impedance change as cells flow through each of the electrodes) will then be processed to obtain cell size and transit time. These data will be used to accurately determine the changes coming purely from the differences in cell stiffness without the influence from cell size variations. Data obtained from measurements using cell lines will be compared to those in the literature.

Sub-Aim 2.3. Perform a test of the cell stiffness analysis system: We will use elastic hydrogel microbeads and different sub-types of neurons to measure the stiffness. Both devices will be first tested for the errorless operation and characterized for their maximum achievable flow speed using elastic hydrogel microbeads (e.g., poly(ethylene glycol) family) having two different sizes (5 and 10 μm) and two different stiffnesses (by changing their polymer composition ratios). Either conventional or microfluidic emulsion process will be utilized to generate microbeads of different sizes. Following this initial characterization, the elasticity of somata of different neuronal cell types will be measured with the proposed biochip and the results validated against data from microfluidic means, conventional micropipette aspiration, and AFM.

Sub-Aim 2.4. Integrate High-throughput Single-Cell Sorting Sub-system into the microfluidic platform: Being able to sort cells based on their elasticity allows downstream confirmation analysis of the cell types through means such as immunostaining (Aim 3). A pneumatically actuated sorting system is easiest to implement (preliminary data shown in Fig. 7A), however it cannot go beyond \sim 100 events/sec. Thus we will build a dielectric microfluidic sorter that can provide faster sorting rates (up to 2000 events/sec has been reported; Mazutis et al. 2013). Fig. 7B shows dielectric sorting of microbeads using our prototype platform. The optimized version of this dielectric sorter will be directly integrated into our microfluidic system (Fig. 6c). Our expected sorting speed is over 2000 events/sec. All microfluidic chips at this stage will be fabricated in poly(dimethyl siloxane) (PDMS) using soft lithography on an electrode-patterned glass substrate.

Sub-Aim 2.5. Survey cell stiffness of neurons and correlate them to neuronal cell-type-related properties: Once the accuracy of our elasticity measurement system is established, we will conduct a large-scale elasticity survey of neurons sampled from key cortical and subcortical areas of the mouse brain. The resulting survey will be correlated with morphological, molecular, and electrophysiological properties of the same type of neurons from Aims 1, 3, and 4.

C.3. Aim 3: Molecular characterization of different morphological cell types

Immunohistochemistry techniques will be used to validate the morphological classes determined in Aim 1. Transgenic animals will be used to contrast broad cell types (such as excitatory vs. inhibitory cell types) and correlate them to morphological characteristics.

We used KESM to scan and reconstruct an entire Nissl-stained mouse brain; thus, we have demonstrated that this technology can easily be scaled-up to reconstruct the locations of large numbers of cells in the entire mouse brain. In order to establish KESM for fluorescence-labeled cells (neurons, glia, endothelial cells etc.) we will use a GAD67-GFP knock-in mouse that expresses enhanced Green Fluorescent Protein (eGFP) in virtually

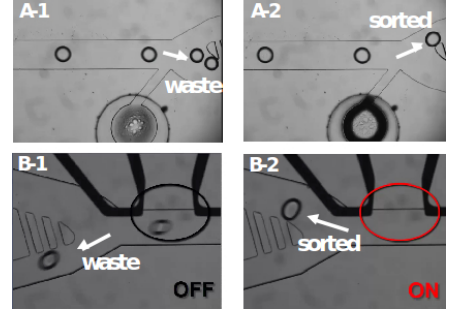


Figure 7: Preliminary Results: Pneumatic sorting vs. Dielectric Sorting Prototype. Cell sorting using pneumatic (A-1, A-2) vs. dielectric methods (B-1, B-2).

all GABAergic neurons positive for GAD67, with little or no expression in non-GABAergic cells (Tamamaki et al. 2003). See Fig. 8 for pilot data. This GAD67-GFP knockin mouse strain allows nearly complete identification of GABAergic neurons in mouse brain, and can be combined with other molecular, functional and morphological markers to characterize neuronal subpopulations. This line will serve as a model system for other transgenic mouse lines expressing eGFP under the control of different gene promoters to describe other distinct cell populations such as excitatory neurons, glia, immune or endothelial cells. Furthermore, this eGFP mouse line can be used to study dendrites and axons to identify connectivity patterns since the transgene fills entire cells, including neuronal dendrites and axons (McKenna et al. 2013; Tamamaki et al. 2003). If this mouse line is not available or staining intensity is not strong enough for direct eGFP fluorescence detection directly, other BAC transgenic mice expressing eGFP under the GAD67 promoter are available (Jackson Labs) and will be tested. In general, these transgenic mouse lines stably express the transgene resulting in expression patterns that are reproducible between individual mice and across generations. We also plan to combine eGFP and retrograde tracing with fluorescent microspheres (Cao et al. 2012) to further characterize the connectome of identified GABAergic neurons.

However, first we need to compare data derived with “conventional” methods such as immunohistochemistry or fluorescence confocal microscopy with those derived from fluorescence KESM (fKESM; see Fig. 9 for preliminary results; cf. Gong et al. 2013). To accomplish this goal, we need to down-scale the analysis to a small brain region because conventional techniques are time consuming, and labor-intensive, and not currently suited for surveying the whole brain. Therefore, we will focus our analysis on the olfactory bulb, which is ideally suited for this purpose. This brain region is easy to identify and small enough so that the entire bulb can be scanned using confocal fluorescence microscopy. Furthermore, this layered brain structure contains excitatory and inhibitory neurons, which are highly connected within the olfactory bulb and with other brain areas. Thus, we can expand our studies to include excitatory neurons and glia cells in future analyses

Sub-Aim 3.1. Comparison of the efficiency of detecting eGFP labeled cells with Fluorescence Confocal Microscopy and fKESM: We will determine the number of cells expressing eGFP in the olfactory bulb and compare them with those derived with fKESM. This step will serve as an initial validation of fKESM. See below for validation based on full geometric reconstructions of these cells.

Sub-Aim 3.2. Identify location of eGFP expressing neurons within a selected brain area: We will use confocal microscopy to reconstruct expression of the transgene in the olfactory bulb to determine their spatial distribution in this structure. We will compare the neuronal expression pattern with those derived with fKESM. This step will allow us to estimate the degree of quenching in fluorescence signal due to polymer embedding for fKESM.

Sub-Aim 3.3. Characterize morphological features of labeled neurons, including information about their dendritic trees and potential connectivity pattern: Neurons expressing eGFP will be morphologically characterized in terms of their shape, size and dendritic morphology and these neuronal characteristics compared with those derived with fKESM. For the cell-type characterization, we will use the Petilla nomenclature which was first developed for cortical interneurons to describe GAD67-eGFP inhibitory neurons in the olfactory bulb (Ascoli et al. 2008).

Sub-Aim 3.4. Combine different molecular markers to identify neuronal subpopulations: We will use combinations of different molecular markers to identify subpopulations of eGFP expressing neurons using double immunohistochemistry (Tamamaki et al. 2003). Results obtained with different molecular markers will be compared with spatial information and morphological parameters to determine which morphological characteristics can be used to identify specific subpopulations. Once we have verified the accuracy of data obtained with fKESM by comparing results derived with conventional confocal microscopy with fKESM, we will be able to scale up to perform reconstruction of the entire mouse brain at micron-scale resolution.

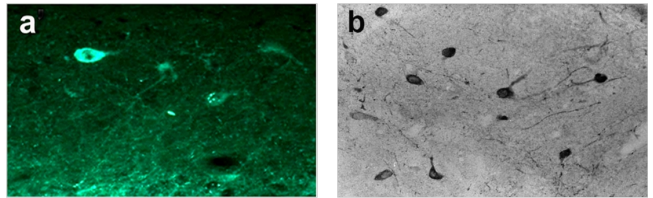


Figure 8: Examples of Immunohistochemistry Staining in Mouse Brain. (a) Fluorescence image of GAD67 immunoreactivity in inhibitory interneurons in the CA1 field of the hippocampus. (b) Lightmicroscopic image of ChAT immunoreactivity in cholinergic neurons in mouse basal forebrain.

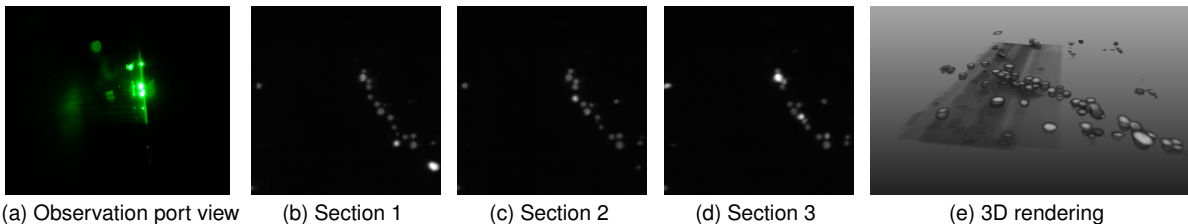


Figure 9: Preliminary Data: Fluorescence Pilot Results Using KESM. Initial fluorescence imaging results using KESM are shown. Fluorescent latex beads ($10\text{ }\mu\text{m}$ diameter) embedded in nitrocellulose were imaged, using 473 nm , 25 mW diode laser line generator (excitation) and Chroma D535/40M 34320 512 nm – 552 nm emission filter. (a) Fluorescence observed through observation port. Scattered latex bead debris can be seen on the knife edge (long vertical bright region in the middle). (b)–(d) Fluorescence beads scanned with KESM. The images appear as grayscale since we are using a monochrome linescan camera. (e) 3D rendering of a small volume including (b)–(d).

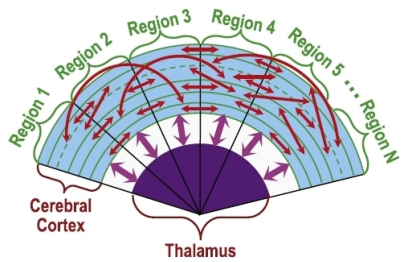
Confocal microscopy: Immunohistochemistry will be performed on fixed $100\text{-}\mu\text{m}$ thick brain sections as described in Ippolito and Eroglu (2010). Fluorescent labeled secondary antibodies will be used, i.e. goat anti guinea-pig Alexa 488 (Life Science Technology) or goat anti-mouse IgG Alexa Fluor94, (Sigma, St. Louis, MO). Images will be acquired using $20\times$ and $100\times$ objectives with oil, at an excitation wavelength of 633 nm with dichotic mirror BS20/80. The emission fluorescence will be collected from 645 – 745 nm . A Z-stack series image will be collected at a step setting of 0.45 section with $100\times$ oil immersion and a sampling speed of 2.0 pixel. Data will be analyzed using FluoViewFv1000 software. Serial reconstruction of the large image-stacks will be done to create a three-dimensional model containing the exact position of all labeled neurons within the OB as described in Kopel et al. (2009).

Description of primary antibodies to be used: For identification of inhibitory GABAergic interneurons we will use a mouse monoclonal anti-GAD67 antibody (MAb) (Millipore, Inc.) with no cross-reactivity with the 65-kDa isoform of GAD, a mouse monoclonal anti-parvalbumin antibody (Millipore, Inc.,) which recognizes a single band of 12 kDa , a monoclonal anti-somatostatin antibody (Abcam, Cambridge, MA, ab37208), a mouse monoclonal anti-calretinin antibody (Millipore, Inc.,) which recognizes a single band with an estimated molecular weight of 31 kDa in line with the expected molecular weight for calretinin. For identification of excitatory neurons, we will use anti-vesicular glutamate transporter 1 and 2 antibodies (Millipore, Inc.).

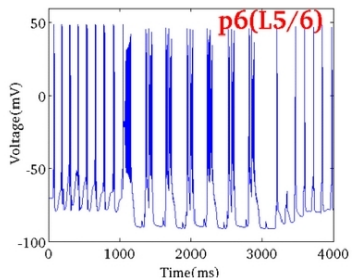
C.4. Aim 4: Computational characterization of different morphological cell types

Characterizing electrophysiological behaviors of the cells is an integrated part of the proposed work. To this end, our main effort will be placed on building biophysically detailed neuronal models (e.g. Hodgkin-Huxley type models), analyzing and characterizing key firing patterns and other behaviors of various cell types. Such cell features are indicative of fundamental properties of the cells pertaining to their neurological functions and information processing capability and hence provide a behavioral classification of cell types. In this project, this behavioral classification will be integrated with other types of classification as targeted in other tasks of this work.

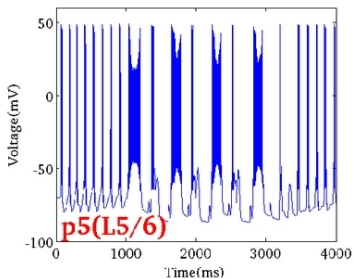
Sub-Aim 4.1. Cell-type classification through multicompartmental simulation using neurons reconstructed from KESM data: We will take a complementary approach to neuronal cell modeling wherein a combination of our own morphological and biophysical data and published experimental data are used. The KESM, when used in conjunction of our automated 3D reconstruction algorithms, offers a promising opportunity to build a large set of biophysically accurate neuronal models using reconstructed morphological data across major cortical and subcortical nuclei. The accuracy of cell modeling (hence the accuracy of behavioral characterization) is a key enabler. To achieve this goal, each cell type will be modeled with high-precision using a large number of compartments. The precision in multi-compartmental neuronal modeling has immediate benefits. While distinct cell morphologies or their variability are the basis of morphological survey of cell types, accurate multi-compartmental cell modeling allows accurate capture of variations in morphology in computer simulation and hence serves as a bridge to electrophysiologically based cell-type survey. In addition to cell classifications based on morphology, biophysical and molecular properties, electrophysiological characterization may lead to additional cell types or



(a) Model

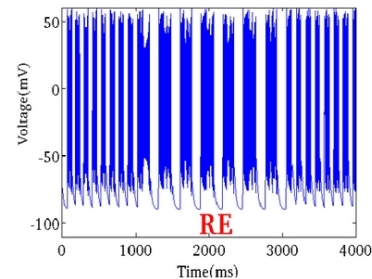


(c) Layer 6 pyramidal cell

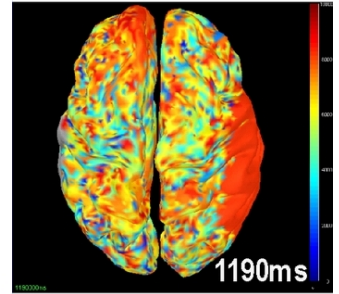


(d) Layer 5 pyramidal cell

(b) Simulated cell types



(e) TRN neuron



1190ms

Figure 10: Preliminary Data: Very Large Scale Brain Modeling and Simulation. Simulation of spike-and-wave seizure activities due to suppression of GABAa receptors is shown. (a) Thalamocortical and corticocortical connectivity model used for the simulation. (b) A table of simulated cell types. Simulated firings of (c) a layer-6 pyramidal cell that projects to layers 5 and 6, (d) a layer-5 pyramidal cell that projects to layers 5 and 6, (e) a thalamic reticular nucleus cell, and (f) simulated post-synaptic current distribution at time 1190 msec (Zhang et al. 2012).

sub-types, providing additional correlated mechanisms for cell classification (cf. Subkhankulova et al. 2010 where the reverse correlation was inferred, from genes to electrophysiology).

Sub-Aim 4.2. Scale up multicompartmental simulation to the whole mouse brain: Co-I Li has extensive experience in biophysically based modeling of neuronal networks, parallel numerical techniques for large-scale simulation of brain models, and computational modeling of epilepsy, and development of parallel neural network simulation tools on multi-core shared memory machines, massively parallel graphic processors and supercomputers (Wang et al. 2011; Yan and Li 2011a,b, 2013; Zhang et al. 2012).

In particular, Li's lab has developed a large-scale biophysically realistic thalamocortical model and an in-house parallel neural network simulator (Zhang et al. 2012). The model consists of a modeled six-layered cerebral cortex with 70 brain regions and multiple thalamic nuclei connected according to global white fiber imaging data. More than 22 types of neurons are characterized using multi-compartmental Hodgkin-Huxley models based on published experimental data. A number of efficient parallel computational techniques have developed in the dedicated simulator to speed up large-scale dynamic simulation. This simulation environment has also been ported to the machines at the Texas A&M Supercomputing Center. This modeling and simulation environment makes it possible to feasibly simulate brain models of more than one million multi-compartmental neurons and hundreds of millions of synapses on a commodity 24-processor server. Such simulations reproduced sigma and delta waves occurring in the early and deep sleep stages, shed light on the role of synaptic characteristics in generating seizures, reveal the firing activities of various cell types (Fig. 10).

Sub-Aim 4.3. Classification of neuronal cell-type based on multicompartmental simulation: Our prior experiences (outlined above) will be leveraged to construct a much larger set of neuronal models as needed in this work. Furthermore, efficient numerical simulation methods and tools will be developed to allow feasible characterization of large numbers of reconstructed cells. To be able to systematically identify cell types and/or sub-types, statistical learning techniques will be adopted/developed to cluster a vast amount of firing behaviors into a reduced set of distinct cell (sub-)types (see e.g., Subkhankulova et al. 2010).

Location	Neuron type	Excitability	Description
Cortex	p2/3	Excitatory	Pyramidal in L2/3
	ss4(L2/3)	Excitatory	Spiny stellate in L4 (project to L2/3)
	ss4(L4)	Excitatory	Spiny stellate in L4
	p4	Excitatory	Pyramidal in L4 (project to L4)
	p5(L2/3)	Excitatory	Pyramidal in L5 (project to L2/3)
	p5(L5/6)	Excitatory	Pyramidal in L5 (project to L5/6)
	p6(L4)	Excitatory	Pyramidal in L6 (project to L4)
	p6(L5/6)	Excitatory	Pyramidal in L6 (project to L5/6)
	b2/3, b4, b5, b6	Inhibitory	Basket interneurons in L2/3/4/5
	nb1, nb2/3, nb4, nb5, nb6	Inhibitory	Nonbasket interneurons in all layers
Thalamus	TC _s /TC _n	Excitatory	Thalamocortical relay cells in specific/nonspecific nucleus
	TI _s /TI _n	Inhibitory	Thalamocortical interneurons in specific/nonspecific nucleus
	RE	Inhibitory	Thalamic reticular cells

C.5. Aim 5: Neuroinformatics platform for the exploration and analysis of data from Aims 1 through 4

We developed the Knife-Edge Scanning Microscope Brain Atlas (KESMBA, <http://kesm.org>), a web-based light-weight data browsing environment, to give users full access to our KESM mouse brain data sets (Chung et al. 2011). The neuroinformatics platform employs 3D rendering based on transparent overlays and distance attenuation (Eng and Choe 2008), only using standard HTML, Javascript, and Cascading Styling Sheets (CSS) to enable a quick, effective, and resource-efficient web-based exploration. Fig. 11 shows screenshots of the platform. We will enrich the KESMBA with morphological, biophysical, molecular, and electrophysiological data from Aims 1 through 4, and enable linkage to third-party resources on mouse brain connectivity (Allen Institute for Brain Science 2012; Hintiryan et al. 2012; Mitra 2012; Zingg et al. 2014) and gene expression (Lein et al. 2007).

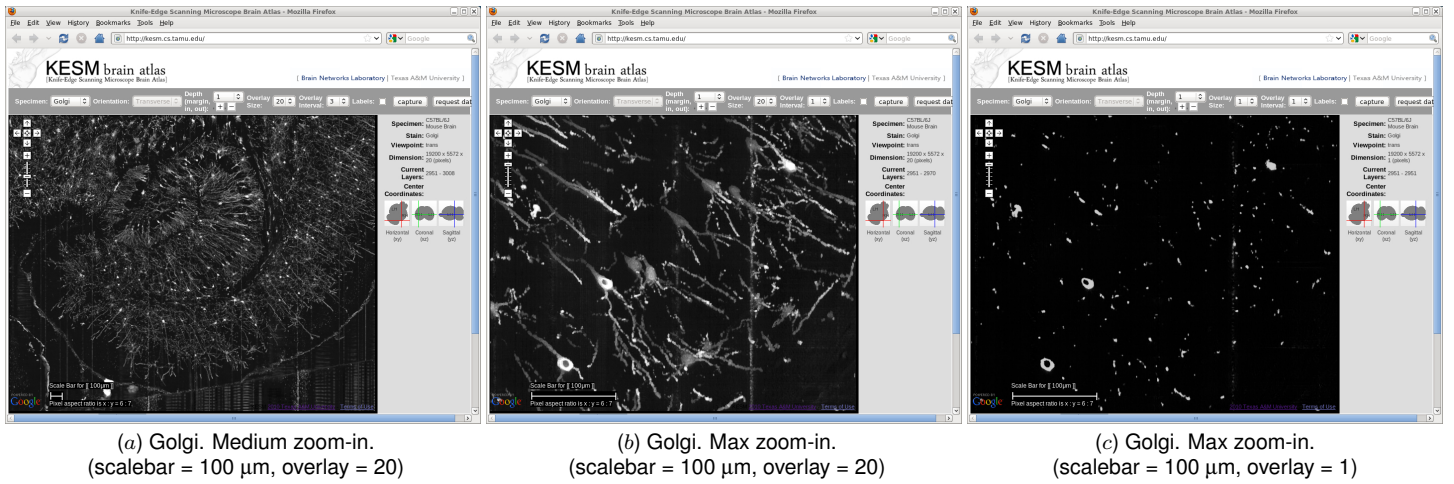


Figure 11: Preliminary Results: KESM Brain Atlas. Screenshots from the KESM Brain Atlas running in the Firefox web browser are shown. (a) Golgi data set at medium zoom-in. Overlay of 20 sections at an interval of 3 (visualized thickness = 60 μm). The spiral-like Dentate gyrus and CA1 in the hippocampus are prominently visible. (b) Golgi data set at max zoom-in. Overlay of 20 sections at an interval of 1 (visualized thickness = 20 μm). Details of the hippocampus is shown. (c) Golgi data set at max zoom-in: same region as (b). A single section is shown (visualized thickness = 1 μm). Viewing individual sections like these does not give much insight, but also note that due to such high z -axis resolution, ambiguities such as fiber crossing can be easily resolved.

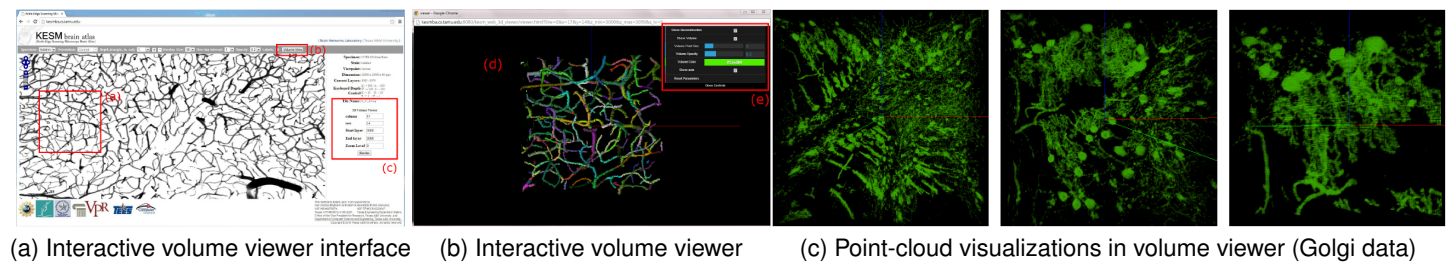


Figure 12: Preliminary Results: WebGL-Based Interactive 3D Volume Viewer. Our prototype implementation of Web-GL-based in-browser interactive 3D volume viewer is shown. (a) Interface in KESMBA to initiate the volume viewer. (b) India ink (vasculature) data being displayed in the volume viewer. Users can interact freely with the data volume (zoom in/out, rotate, translate). Here, reconstruction results are shown in color, along with basic statistics (box on the right). (c) Golgi data: point-cloud visualization only (no reconstruction).

Sub-Aim 5.1. Integrate reconstructed neuronal morphology and cell-type annotations into the KESM Brain Atlas: In this aim, we will build up on KESMBA to include overlays of reconstructed neuronal morphology and cell-type annotations. We will use standard vector graphics overlaying API calls to achieve this. Furthermore, we will enable querying for specific cell-type-specific properties and their summary statistics. The properties will include morphological, electrical, biophysical, and molecular characteristics. We will also use WebGL to develop

a fully interactive, in-browser 3D volume viewer. Fig. 12 shows our prototype with limited 3D reconstruction and morphometric statistics display capability.

Sub-Aim 5.2. Generate whole-brain statistical distribution maps of cell-type-specific properties: With the KESM Golgi data and the fully reconstructed neuronal morphologies, we can generate a high-resolution heatmap based on specific morphometric and other cell-type-specific. For example, we can generate a 3D map where certain types (or sub-types) of neurons more commonly occur. Such morphometric or cell-type-specific property distribution maps can provide valuable clues for discovering new cell types or sub-types and also for inferring function of specific cell types (see Sub-Aim 5.3). These distribution maps can be interpreted as probability densities (or probability masses), thus they enable statistical measures like the Kullback-Liebler (KL) divergence (Kullback and Leibler 1951).

Sub-Aim 5.3. Correlate distribution of cell-type-specific properties to connectivity and gene expression atlases:

Morphometric and cell-type distribution maps can be used to query existing 3D gene expression atlases such as the ABA (Lein et al. 2007) to find genes that control certain geometric properties of neurons or to infer functional properties of the queried cell types. Furthermore, we will incorporate long-range projection data from third-party sources (Allen Institute for Brain Science 2012; Hintiryan et al. 2012; Mitra 2012; Zingg et al. 2014). We are currently using local deformation-based registration methods that employ Moving Least Squares (Schaefer et al. 2006). We have already started our preliminary work on registering KESMBA to the ABA reference atlas (Fig. 13). We will extend on this approach for atlas-to-atlas registration. Once we register our data to the over 20,000 different gene expression data sets in the ABA collection. Using KL divergence and other measures, we expect to map morphometric distributions to genetic/molecular distributions. On the other hand, linking with connectivity atlases will allow us to construct whole brain simulations (as in Fig. 10), however such a full simulation is beyond the scope of our project so we will leave it for future investigations.

D. Milestones, Timeline, and Project Management

The milestones and timelines of this project are summarized below, organized along the required goals of this Funding Opportunity Announcement (FOA). Milestones to be achieved in two phases are marked accordingly. For PI/Co-I responsibilities and timeline, see the budget justification under “Senior Personnel”.

Table 1: Milestones and Timeline

Task	Year 1	Year 2	Year 3	Aims
(1) Define and provide cell classification data in the whole brain, brain regions, or significant functional circuitry in the vertebrate nervous system				
- brain-wide neuronal morphology				Aim 1
- select biophysical properties (elasticity, stiffness)				Aim 2
- select transgene and molecular properties				Aim 3
- brain-wide electrophysiological prop. (multicompartmental models)				Aim 4
(2) Integrate info. on the molecular id. of cell types with conn., morphology, location, and/or other cell type characteristics with functional significance				
- Correlate morphology and molecular properties				Aims 1, 3
- Correlate morphology, biophysical, and electrophysiological prop.				Aims 1, 2, 4
(3) Apply statistical methods for creating a taxonomy of cell types based on molecular identity and connectivity				
- Correlate morphometric distribution maps to mole. and gene expr. data				Aim 5 (data from Aims 1, 3)
(4) Provide realistic estimates on the number/percentage of defined cell types in specific region(s) and/or circuit(s)				
- Estimate brain-wide distribution maps of cell-type-specific prop.				Aim 5 (data from Aims 1–4)
(5) Provide a basis to map cell types based on molecular identity and connectivity onto a reference brain atlas				
- Map KESM brain atlas + cell-type-specific properties to Allen atlas				Aim 5 (data from Aims 1–4)
(6) Demonstrate broader utility and scalability to establish the feasibility of applying these approaches to an entire brain				
- Make public KESM brain atlas + cell-type-specific properties				Aim 5

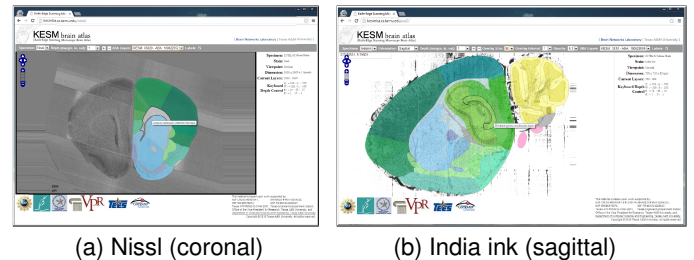


Figure 13: **Preliminary Results: Registration of KESM Brain Atlas to the Allen Reference Atlas.** Registration of KESM Nissl (a) and India ink data (b) to the Allen Reference Atlas. The results are based on semi-automated linear registration. Rich annotations from the Allen Reference Atlas are visible.

Bibliography and References Cited

Allen Institute for Brain Science (2012). ALLEN mouse brain connectivity atlas technical white paper: Overview. Technical Report October 2012 v.4, Allen Institute for Brain Science. <http://connectivity.brain-map.org>.

Anderson, J. R., Jones, B. W., Watt, C. B., Shaw, M. V., Yang, J.-H., DeMill, D., Lauritzen, J. S., Lin, Y., Rapp, K. D., Mastronarde, D., Koshevoy, P., , Grimm, B., Tasdizen, T., , Whitaker, R., , and Marc, R. E. (2011). Exploring the retinal connectome. *Molecular Vision*, 17:355–379.

Ascoli, G. A., Alonso-Nanclares, L., Anderson, S. A., Barrionuevo, G., Benavides-Piccione, R., Burkhalter, A., Buzsáki, G., Cauli, B., DeFelipe, J., Fairén, A., Feldmeyer, D., Fishell, G., Fregnac, Y., Freund, T. F., Gardner, D., Gardner, E. P., Goldberg, J. H., Helmstaedter, M., Hestrin, S., Karube, F., Kisvárday, Z. F., Lambolez, B., Lewis, D. A., Marin, O., Markram, H., Muñoz, A., Packer, A., Petersen, C. C. H., Rockland, K. S., Rossier, J., Rudy, B., Somogyi, P., Staiger, J. F., Tamas, G., Thomson, A. M., Toledo-Rodriguez, M., Wang, Y., West, D. C., and Yuste, R. (2008). Petilla terminology: nomenclature of features of GABAergic interneurons of the cerebral cortex. *Nature Reviews Neuroscience*, 9:557–568. For the Petilla Interneuron Nomenclature Group (PING).

Boldak, C., Rolland, Y., and Toumoulin, C. (2003). An improved model-based vessel tracking algorithm with application to computed tomography angiography. *Journal of Biocybernetics and Biomedical Engineering*, 3:41–64.

Bota, M., Sporns, O., and Swanson, L. W. (2012). Neuroinformatics analysis of molecular expression patterns and neuron populations in gray matter regions: The rat bst as a rich exemplar. *Brain research*, 1450:174–193.

Bota, M., and Swanson, L. W. (2007). The neuron classification problem. *Brain research reviews*, 56:79–88.

Bow, H., Pivkin, I. V., Diez-Silva, M., Goldfless, S. J., Dao, M., Niles, J. C., Suresh, S., and Han, J. (2011). A microfabricated deformability-based flow cytometer with application to malaria. *Lab on a Chip*, 11:1065–1073.

Bullmore, E., and Sporns, O. (2009). Complex brain networks: graph theoretical analysis of structural and functional systems. *Nature Reviews Neuroscience*, 10:186–198.

Cao, J., Naito, J., and Chen, Y. (2012). Retrograde tracing with fluorescent microspheres reveals bifurcating projections from central retina to tectum and thalamus in chicks. *Anatomia, histologia, embryologia*, 41:306–310.

Cho, Y., Kim, H. S., Bruno Frazier, A., Chen, Z. G., Shin, D. M., and Han, A. (2009). Whole-cell impedance analysis for highly and poorly metastatic cancer cells. *Microelectromechanical Systems, Journal of*, 18:808–817.

Choe, Y., Mayerich, D., Kwon, J., Miller, D. E., Sung, C., Chung, J. R., Huffman, T., Keyser, J., and Abbott, L. C. (2011). Specimen preparation, imaging, and analysis protocols for knife-edge scanning microscopy. *Journal of Visualized Experiments*, 58:e3248. Doi: 10.3791/3248.

Chung, J. R., Sung, C., Mayerich, D., Kwon, J., Miller, D. E., Huffman, T., Abbott, L. C., Keyser, J., and Choe, Y. (2011). Multiscale exploration of mouse brain microstructures using the knife-edge scanning microscope brain atlas. *Frontiers in Neuroinformatics*, 5:29.

Cross, S. E., Jin, Y.-S., Rao, J., and Gimzewski, J. K. (2007). Nanomechanical analysis of cells from cancer patients. *Nature nanotechnology*, 2:780–783.

Denk, W., and Horstmann, H. (2004). Serial block-face scanning electron microscopy to reconstruct three-dimensional tissue nanostructure. *PLoS Biology*, 19:e329.

- Eng, D. C.-Y., and Choe, Y. (2008). Stereo pseudo 3D rendering for web-based display of scientific volumetric data. In *Proceedings of the IEEE/EG International Symposium on Volume Graphics*.
- Fishell, G., and Heintz, N. (2013). The neuron identity problem: Form meets function. *Neuron*, 80:602–612.
- Frangi, A. F., Niessen, W. J., Hoogeveen, R. M., Walsum, T. V., and Viergever, M. A. (1999). Model-based quantification of 3-D magnetic resonance angiographic images. *IEEE Transactions on Medical Imaging*, 18:946–956.
- Gleeson, P., Crook, S., Cannon, R. C., Hines, M. L., Billings, G. O., Farinella, M., Morse, T. M., Davison, A. P., Ray, S., Bhalla, U. S., et al. (2010). Neuroml: a language for describing data driven models of neurons and networks with a high degree of biological detail. *PLoS computational biology*, 6:e1000815.
- Gong, H., Zeng, S., Yan, C., Lv, X., Yang, Z., Xu, T., Feng, Z., Ding, W., Qi, X., Li, A., et al. (2013). Continuously tracing brain-wide long-distance axonal projections in mice at a one-micron voxel resolution. *Neuroimage*, 74:87–98.
- Hagmann, P., Cammoun, L., Gigandet, X., Meuli, R., Honey, C. J., Wedeen, V. J., and O.Sporns (2008). Mapping the structural core of human cerebral cortex. *PLoS Biology*, 6:e159.
- Hagmann, P., Kurant, M., Gigandet, X., Thiran, P., Wedeen, V. J., Meuli, R., and Thiran, J.-P. (2007). Mapping human whole-brain structural networks with diffusion MRI. *PLoS ONE*, 2:e597.
- Halavi, M., Polavaram, S., Donohue, D. E., Hamilton, G., Hoyt, J., Smith, K. P., and Ascoli, G. A. (2008). Neuromorpho.org implementation of digital neuroscience: dense coverage and integration with the nif. *Neuroinformatics*, 6:241–252.
- Han, A., Graff, M., Wang, O., and Frazier, A. B. (2005). An approach to multilayer microfluidic systems with integrated electrical, optical, and mechanical functionality. *Sensors Journal, IEEE*, 5:82–89.
- Han, A., Yang, L., and Frazier, A. B. (2007). Quantification of the heterogeneity in breast cancer cell lines using whole-cell impedance spectroscopy. *Clinical cancer research*, 13:139–143.
- Han, D., Choi, H., Park, C., and Choe, Y. (2009a). Fast and accurate retinal vasculature tracing and kernel-isomap-based feature selection. In *Proceedings of the International Joint Conference on Neural Networks*, 1075–1082. Piscataway, NJ: IEEE Press.
- Han, D., Keyser, J., and Choe, Y. (2009b). A local maximum intensity projection tracing of vasculature in Knife-Edge Scanning Microscope volume data. In *Proceedings of the IEEE International Symposium on Biomedical Imaging*, 1259–1262.
- Hayworth, K. J., Kasthuri, N., Schalek, R., and Lichtman, J. W. (2006). Automating the collection of ultrathin sections for large volume TEM reconstructions. *Microscopy and Microanalysis*, 12(Suppl. S02):86–87.
- Helmstaedter, M., Briggman, K. L., Turaga, S. C., Jain, V., Seung, H. S., and Denk, W. (2013). Connectomic reconstruction of the inner plexiform layer in the mouse retina. *Nature*, 500:168–174.
- Hennessy, R., Koo, C., Ton, P., Han, A., Righetti, R., and Maitland, K. C. (2011). Particle velocity measurements with macroscopic fluorescence imaging in lymph tissue mimicking microfluidic phantoms. In *SPIE BioS*, 78920R–78920R. International Society for Optics and Photonics.
- Hill, S. L., Wang, Y., Riachi, I., Schürmann, F., and Markram, H. (2012). Statistical connectivity provides a sufficient foundation for specific functional connectivity in neocortical neural microcircuits. *Proceedings of the National Academy of Sciences*, 109:E2885–E2894.
- Hintiryan, H., Gou, L., Zingg, B., Yamashita, S., Lyden, H. M., Song, M. Y., Grewal, A. K., Zhang, X., Toga, A. W., and Dong, H.-W. (2012). Comprehensive connectivity of the mouse main olfactory bulb: Analysis and online digital atlas. *Frontiers in Neuroanatomy*, 6(30).

- Hochmuth, R. M. (2000). Micropipette aspiration of living cells. *Journal of biomechanics*, 33:15–22.
- Ingber, D. E. (2003). Mechanobiology and diseases of mechanotransduction. *Annals of medicine*, 35:564–577.
- Ippolito, D. M., and Eroglu, C. (2010). Quantifying synapses: an immunocytochemistry-based assay to quantify synapse number. *Journal of visualized experiments: JoVE*, (45):2270.
- Johansen-Berg, H., and Rushworth, M. F. (2009). Using diffusion imaging to study human connectional anatomy. *Annual review of neuroscience*, 32:75–94.
- Keller, P. J., Schmidt, A. D., Wittbrodt, J., , and Stelzer, E. H. K. (2008). Reconstruction of zebrafish early embryonic development by scanned light sheet microscopy. *Science*, 322:1065–1069.
- Kim, W., and Han, A. (2011). A micro-aspirator chip using vacuum expanded microchannels for high-throughput mechanical characterization of biological cells. In *Proceedings of the 14th International Conference on Miniaturized Systems for Chemistry and Life Sciences (MicroTAS 2010)*, 253–255.
- Kopel, H., Meshulam, M., and Mizrahi, A. (2009). Three-dimensional distribution patterns of newborn neurons in the adult olfactory bulb. *Journal of neuroscience methods*, 182(2):189–194.
- Kullback, S., and Leibler, R. A. (1951). On information and sufficiency. *The Annals of Mathematical Statistics*, 22:79–86.
- Labarre, D., Meissner, W., and Boraud, T. (2008). Measure of the regularity of events in stochastic point processes, application to neuron activity analysis. In *Acoustics, Speech and Signal Processing, 2008. ICASSP 2008. IEEE International Conference on*, 489–492.
- Larson, S. D., and Martone, M. E. (2013). Neurolex. org: an online framework for neuroscience knowledge. *Frontiers in neuroinformatics*, 7.
- Lein, E. S., Hawrylycz, M. J., Ao, N., Ayres, M., Bensinger, A., Bernard, A., Boe, A. F., Boguski, M. S., Brockway, K. S., Byrnes, E. J., et al. (2007). Genome-wide atlas of gene expression in the adult mouse brain. *Nature*, 445:168–176.
- Li, A., Gong, H., Zhang, B., Wang, Q., Wan, C., Wu, J., Liu, Q., Zeng, S., and Luo, Q. (2010). Micro-optical sectioning tomography to obtain a high-resolution atlas of the mouse brain. *Science*, 330:1404–1408.
- López-Cruz, P. L., Larrañaga, P., DeFelipe, J., and Bielza, C. (2014). Bayesian network modeling of the consensus between experts: An application to neuron classification. *International Journal of Approximate Reasoning*, 55:3–22.
- Markram, H. (2006). The blue brain project. *Nature Reviews Neuroscience*, 7:153–160.
- Mayerich, D., Abbott, L. C., and Keyser, J. (2008a). Visualization of cellular and microvessel relationships. *IEEE Transactions on Visualization and Computer Graphics*, 14:1611–1618.
- Mayerich, D., Abbott, L. C., and McCormick, B. H. (2008b). Knife-edge scanning microscopy for imaging and reconstruction of three-dimensional anatomical structures of the mouse brain. *Journal of Microscopy*, 231:134–143.
- Mayerich, D., and Keyser, J. (2008). Filament tracking and encoding for complex biological networks. In *Proceedings of ACM Symposium on Solid and Physical Modeling*, 353–358.
- Mayerich, D., and Keyser, J. (2009). Hardware accelerated segmentation of complex volumetric filament networks. *IEEE Transactions on Visualization and Computer Graphics*, 15:670–681.
- Mayerich, D., Kwon, J., Choe, Y., Abbott, L., and Keyser, J. (2008c). Constructing high-resolution microvascular models. In *Proceedings of the 3rd International Workshop on Microscopic Image Analysis with Applications in Biology (MIAAB 2008)*. Online.

- Mazutis, L., Gilbert, J., Ung, W. L., Weitz, D. A., Griffiths, A. D., and Heyman, J. A. (2013). Single-cell analysis and sorting using droplet-based microfluidics. *Nature protocols*, 8(5):870–891.
- McCormick, B. H. (2003). The knife-edge scanning microscope. Technical report, Department of Computer Science, Texas A&M University. <http://research.cs.tamu.edu/bnl/>.
- McCormick, B. H. (2004). System and method for imaging an object. USPTO patent #US 6,744,572 (for Knife-Edge Scanning; 13 claims).
- McCormick, B. H., and Mayerich, D. M. (2004). Three-dimensional imaging using Knife-Edge Scanning Microscope. *Microscopy and Microanalysis*, 10 (Suppl. 2):1466–1467.
- McKenna, J. T., Yang, C., Franciosi, S., Winston, S., Abarr, K. K., Rigby, M. S., Yanagawa, Y., McCarley, R. W., and Brown, R. E. (2013). Distribution and intrinsic membrane properties of basal forebrain gabaergic and parvalbumin neurons in the mouse. *Journal of Comparative Neurology*, 521:1225–1250.
- Mel, B. W. (1994). Information processing in dendritic trees. *Neural Computation*, 6:1031–1085.
- Melek, Z., Mayerich, D., Yuksel, C., and Keyser, J. (2006). Visualization of fibrous and thread-like data. *IEEE Transactions on Visualization and Computer Graphics*, 12(5):1165–1172.
- Mitra, P. P. (2012). Technical white paper: Mouse brain architecture project. Technical report, Cold Spring Harbor Laboratory. <http://brainarchitecture.org>.
- Perin, R., Berger, T. K., and Markram, H. (2011). A synaptic organizing principle for cortical neuronal groups. *Proceedings of the National Academy of Sciences*, 108:5419–5424.
- Pham, D. L., Xu, C., and Prince, J. L. (2000). Current methods in medical image segmentation. *Annual Review of Biomedical Engineering*, 2:315–337.
- Ragan, T., Kadiri, L. R., Venkataraju, K. U., Bahlmann, K., Sutin, J., Taranda, J., Arganda-Carreras, I., Kim, Y., Seung, H. S., and Osten, P. (2012). Serial two-photon tomography for automated *ex vivo* mouse brain imaging. *Nature Methods*, 9:255–258.
- Rall, W. (1962). Theory of physiological properties of dendrites. *Annals of the New York Academy of Science*, 96:1071–1092.
- Rall, W., and Agmon-Snir, H. (1998). Cable theory for dendritic neurons. In Koch, C., and Segev, I., editors, *Methods in Neuronal Modeling: From Ions to Networks*, 27–92. Cambridge, MA: MIT Press. Second edition.
- Ramón y Cajal, S. (1995). *Histology of the Nervous System*. New York: Oxford. Translated by N. Swanson and L. W. Swanson.
- Rubinov, M., and Sporns, O. (2010). Complex network measures of brain connectivity: uses and interpretations. *Neuroimage*, 52:1059–1069.
- Schaefer, S., McPhail, T., and Warren, J. (2006). Image deformation using moving least squares. *ACM Transactions on Graphics*, 25(3):533–540.
- Subkhankulova, T., Yano, K., Robinson, H. P., and Livesey, F. J. (2010). Grouping and classifying electrophysiologically-defined classes of neocortical neurons by single cell, whole-genome expression profiling. *Frontiers in molecular neuroscience*, 3.
- Suresh, S. (2007). Nanomedicine: elastic clues in cancer detection. *Nature Nanotechnology*, 2:748–749.
- Swanson, L. W., and Bota, M. (2010). Foundational model of structural connectivity in the nervous system with a schema for wiring diagrams, connectome, and basic plan architecture. *Proceedings of the National Academy of Sciences*, 107:20610–20617.

Tamamaki, N., Yanagawa, Y., Tomioka, R., Miyazaki, J.-I., Obata, K., and Kaneko, T. (2003). Green fluorescent protein expression and colocalization with calretinin, parvalbumin, and somatostatin in the gad67-gfp knock-in mouse. *Journal of Comparative Neurology*, 467:60–79.

Toledo-Rodriguez, M., Blumenfeld, B., Wu, C., Luo, J., Attali, B., Goodman, P., and Markram, H. (2004). Correlation maps allow neuronal electrical properties to be predicted from single-cell gene expression profiles in rat neocortex. *Cerebral Cortex*, 14:1310–1327.

Tsai, P. S., Friedman, B., Ifarraguerri, A. I., Thompson, B. D., Lev-Ram, V., Schaffer, C. B., Xiong, Q., Tsien, R. Y., Squier, J. A., and Kleinfeld, D. (2003). All-optical histology using ultrashort laser pulses. *Neuron*, 39:27–41.

Van Essen, D., Ugurbil, K., Auerbach, E., Barch, D., Behrens, T., Bucholz, R., Chang, A., Chen, L., Corbetta, M., Curtiss, S., Penna, S. D., Feinberg, D., Glasser, M., Harel, N., Heath, A., Larson-Prior, L., Marcus, D., Michalareas, G., Moeller, S., Oostenveld, R., Petersen, S., Prior, F., Schlaggar, B., Smith, S., Snyder, A., Xu, J., and Yacoub, E. (2012). The human connectome project: A data acquisition perspective. *NeuroImage*, 62(4):2222 – 2231.

Wang, M., Yan, B., Hu, J., and Li, P. (2011). Simulation of large neuronal networks with biophysically accurate models on graphics processors. In *Neural Networks (IJCNN), The 2011 International Joint Conference on*, 3184–3193. IEEE.

Warfield, S. J., Zou, K. H., and Wells, W. M. (2002). Validation of image segmentation and expert quality with expectation-minimization algorithm. In *Lecture Notes In Computer Science, Vol. 2488; Proceedings of the 5th International Conference on Medical Image Computing and Computer-Assisted Intervention*, 298–306.

Williams, R. W. (2000). Mapping genes that modulate mouse brain development: a quantitative genetic approach. In Goffinet, A. F., and Rakic, P., editors, *Mouse Brain Development*, 2149. New York: Springer.

Woolsey, T. A., Dierker, M. L., and Wann, D. F. (1975). Mouse smi cortex: Qualitative and quantitative classification of golgi-impregnated barrel neurons. *Proceedings of the National Academy of Sciences*, 72:2165–2169.

Wouterlood, F. G., Boekel, A. J., Kajiwara, R., and Beliën, J. A. (2008). Counting contacts between neurons in 3d in confocal laser scanning images. *Journal of neuroscience methods*, 171:296–308.

Yan, B., and Li, P. (2011a). An integrative view of mechanisms underlying generalized spike-and-wave epileptic seizures and its implication on optimal therapeutic treatments. *PloS one*, 6(7):e22440.

Yan, B., and Li, P. (2011b). Reduced order modeling of passive and quasi-active dendrites for nervous system simulation. *Journal of computational neuroscience*, 31(2):247–271.

Yan, B., and Li, P. (2013). The emergence of abnormal hypersynchronization in the anatomical structural network of human brain. *Neuroimage*, 65:34–51.

Yoo, T., Ackerman, N. J., and Vannier, M. (2000). Toward a common validation methodology for segmentation and registration algorithms. In *Lecture Notes In Computer Science, Vol. 1935; Proceedings of the Third International Conference on Medical Image Computing and Computer-Assisted Intervention*, 422–431. London: Springer.

Zawadzki, K., Miazaki, M., Viana, M., Taraskin, S., et al. (2009). Unveiling the neuromorphological space. *Frontiers in computational neuroscience*, 4:150–150.

Zhang, Y., Yan, B., Wang, M., Hu, J., Lu, H., and Li, P. (2012). Linking brain behavior to underlying cellular mechanisms via large-scale brain modeling and simulation. *Neurocomputing*, 97:317–331.

Zingg, B., Hintiryan, H., Gou, L., Song, M. Y., Bay, M., Bienkowski, M. S., Foster, N. N., Yamashita, S., Bowman, I., Toga, A. W., et al. (2014). Neural networks of the mouse neocortex. *Cell*, 156(5):1096–1111.